THE FU ORIONIS BINARY SYSTEM RNO 1B/1C

STUART MCMULDROCH AND GEOFFREY A. BLAKE

Division of Geological and Planetary Sciences, 170–25, California Institute of Technology, Pasadena, California 91125
Electronic mail: sxm@sol1.gps.caltech.edu, gab@csardas.gps.caltech.edu

ANNEILA I. SARGENT

Division of Physics, Mathematics, and Astronomy, California Institute of Technology, 105–24, Pasadena, California 91125
Electronic mail: afs@mmstar.caltech.edu

Received 1994 June 8; revised 1994 September 19

ABSTRACT

Observations of CS (7→6) emission reveal a $\geq 3 M_\odot$ core, 1.8×10^4 AU in size, surrounding the FU Orionis binary system RNO 1B/1C. Fractional chemical abundances, calculated from LVG and LTE codes, are mostly similar to those in the cold core TMC 1. However, values for SiO/H_2 and CH_3OH/H_2 are enhanced, possibly by sputtering reactions or grain–grain collisions in the outflow associated with the young stars. Aperture synthesis maps of the 2.6 and 3.1 mm continuum emission at ~5″ and ~9″ resolution, respectively, reveal that RNO 1C is surrounded by a flattened, dusty envelope, ~5000 AU in size, with mass $\geq 1.1\ M_\odot$. High spatial resolution (~3″) interferometer observations of CS (2→1) emission may trace the dense walls of an outflow cavity comprised of two concentric arcs with dynamical ages of 4×10^3 and 1×10^4 yr. The velocity structure of lower density gas imaged in the CO (1→0) transition is consistent with the arcs being formed by two energetic FU Orionis outbursts. Each event may have imparted more than 4 $M_\odot$ km s^{-1} to the outflow, implying outburst mass loss rates of $\sim10^{-4}\ M_\odot\ yr^{-1}$. It appears that RNO 1C is probably the driving source for the outflow and that, while pre-main sequence stars are in the FU Orionis stage, outbursts may dominate both outflow morphology and energetics.

1. INTRODUCTION

FU Orionis objects (FUors) may represent a pivotal stage in the evolution of solar mass pre-main sequence stars. They are characterized by a sudden increase in visual brightness of 5–6 mag with a much slower decline, and possess distinctive spectral signatures; the H_α and Na I D lines exhibit P Cygni profiles with a suppressed emission component, while absorption linewidths and spectral type vary with wavelength and often show a "double-peaked" structure (Herbig 1977, 1989; Hartmann & Kenyon 1987; Welty *et al.* 1992; Hartmann *et al.* 1993). FUors also display distinctive arcuate reflection nebulae and large infrared excesses (Goodrich 1987). Many of their observed properties have been interpreted in terms of an elevated rate of accretion through a circumstellar disk onto a T Tauri star (Hartmann & Kenyon 1985, 1987). The number of detected FUor outbursts suggests the phenomenon is repetitive, with stars in the T Tauri stage of evolution undergoing up to 100 outbursts over $\sim10^6$ yr (Herbig 1977, 1989; Hartmann 1992). This hypothesis is supported by observations of outflows from young stellar objects (Reipurth 1992; McMuldroch *et al.* 1993).

The main core of the dark cloud L1287, located some 850 pc distant, contains the cometary nebula GN 00.33.9 (Yang *et al.* 1991). Within this nebula lies the proposed binary FUor system, RNO 1B and RNO 1C (Staude & Neckel 1991; Kenyon *et al.* 1993). The binary components are separated by 6″ at PA~45°. Staude & Neckel (1991) first identified the heavily extincted RNO 1B (A_v~9 mag) as a FUor and suggested that a nearby bright knot that they designated RNO 1C might contain an even more deeply embedded star. This knot was subsequently identified as a FUor (Kenyon *et al.* 1993). Both objects lie within the positional error bars of IRAS 00338+6312 ($L\sim680L_\odot$) and are associated with water masers (Fiebig *et al.* 1992).

Single dish ammonia observations reveal a rotating core, ~0.5×0.2 pc in size and elongated along PA 135°, around the FUors (Estalella *et al.* 1993). Maps in the CO (1→0), HCO^+ (1→0), and CO (3→2) transitions indicate that the driving source(s) for an energetic bipolar outflow, oriented at PA~45° and situated within 30° of the plane of the sky, lie within this core (Snell *et al.* 1990; Yang *et al.* 1991; Evans *et al.* 1994). Infrared polarimetric imaging (Weintraub & Kastner 1993) suggests that the source of the outflow is closer to the nominal position of IRAS 00338+6312 than RNO 1B or RNO 1C. A VLA map of the 3.6 cm continuum emission also displays a peak within 1″ of the IRAS position and has been interpreted as confirming the presence of a driving source quite distinct from the FUors (Anglada *et al.* 1994).

Although ~7″ resolution aperture synthesis images of CS (2→1) show an intensity maximum near the *IRAS* position, they lack the sensitivity and spatial resolution to delineate structure reliably (Yang *et al.* 1993). To clarify the detailed structure of the L1287 core, and as part of a larger project to examine FUor characteristics (McMuldroch *et al.* 1993), we have undertaken a program of sensitive high resolution millimeter and submillimeter observations using the Owens Valley millimeter array and the Caltech Submillimeter Observatory, the results of which we describe below.

 0004-6256/95/110(1)/354/12/$0.90

TABLE 1. CSO observations.

(1) Molecule	(2) Transition	(3) ν (GHz)	(4) Peak T (K)	(5) FWHM (kms^{-1})	(6) Velocity (kms^{-1})	(7) $\int T dv$ (K kms^{-1})	(8) Wings	(9) N (cm^{-2})	(10) $F_{C^{18}O}$[1]	(11) F_{CO}[2]	(12) F_{TMC1}
SiO	5→4	217.105	0.3	2.9	-15.7	0.7	?	1(12)	1(-11)	5(-10)	2(-12)
H_2CO	$3_{0,3} \rightarrow 2_{0,2}$	218.222	3.1	4.1	-17.6	14.0	blue	1(14)	1(-9)	5(-8)	2(-8)
CH_3OH	$4_2 \rightarrow 3_1$	218.440	0.71	3.1	-17.4	2.3	?	4(14)	4(-9)	2(-7)	2(-9)
H_2CO	$3_{2,2} \rightarrow 2_{2,1}$	218.475	0.6	3.4	-16.9	2.6	?	2(14)	2(-9)	1(-7)	2(-8)
$C^{18}O$	2→1	219.560	4.96	3.34	-18.3	20.0	no	2(16)	2(-7)	–	2(-7)
SO	$5_6 \rightarrow 4_5$	219.949	1.5	2.7	-17.2	6.0	blue	7(13)	7(-10)	4(-8)	5(-9)
^{13}CO	2→1	220.399	15.9	3.30	-18.6	69.0	blue	1(17)	1(-6)	5(-5)	1(-6)
CO	2→1	230.538	32.9	–	–	–	strong	–	–	–	
CS	7→6	342.883	1.9	3.3	-17.0	8.8	weak	2(14)	2(-9)	1(-7)	1(-8)
CO	3→2	345.796	25.8	–	–	–	strong	–	–	–	
HCN	4→3	354.505	2.5	5.2	-16.4	15.5	yes	1(14)	1(-9)	5(-8)	2(-8)
HCO^+	4→3	356.734	8.8	–	–	–	yes	–	–	–	

Notes to TABLE 1

(1) The fractional abundance relative to H_2 derived using the $C^{18}O$ column density. (2) The fractional abundance relative to H_2 derived using the CO column density.

2. OBSERVATIONS

2.1 CSO Observations

Observations of the core of L1287, encompassing RNO 1B, RNO 1C, and IRAS 00338+6312, were acquired with the Caltech Submillimeter Observatory (CSO) on Mauna Kea, Hawaii, in 1991 July. The facility 230 and 345 GHz SIS heterodyne receivers were used in conjunction with the CSO 500 and 50 MHz bandwidth acousto-optical spectrometers (Ellison & Miller 1987; Ellison *et al.* 1989). Calibration was accomplished by the standard chopper wheel method, while main beam efficiencies were calculated to approximately 20% accuracy from measurements of Jupiter. At 230 and 345 GHz, the beamwidths were 31″ and 21″ (FWHM), with main beam efficiencies of 0.52 and 0.58, respectively. All temperatures quoted in the paper have been corrected for these main beam efficiencies. Position switching to a reference position 10′ west of RNO 1B produced the least contaminated baselines. Pointing was checked regularly on planets and nearby point sources; absolute positions are accurate to within 10″, relative positions within the maps to ~5″.

Several molecular species were detected towards RNO 1B in the 230 and 345 GHz bands and are listed in Table 1. Spectra were acquired for the CO (2→1), $C^{18}O$ (2→1), SiO (5→4), SO ($5_6 \rightarrow 4_5$), HCN (4→3), CH_3OH ($4_2 \rightarrow 3_1$), HCO^+ (4→3), H_2CO ($3_{0,3} \rightarrow 2_{0,2}$), and H_2CO ($3_{2,2} \rightarrow 2_{2,1}$) rotational transitions. In addition, ^{13}CO (2→1) emission at 220 GHz was mapped at half beam spacings over a region ~45″×45″ in size. More extensive maps, ~80″×80″, also sampled at half beam spacings, were made of the CO (3→2) and CS (7→6) emission. Due to their small Einstein A coefficients, CO and ^{13}CO trace relatively cold, low density gas while CS, with its higher dipole moment, delineates higher density gas.

2.2. OVRO Observations

Aperture synthesis mapping of the $J=1 \rightarrow 0$ transition of ^{12}CO and the $J=2 \rightarrow 1$ transition of CS at $\nu=115.271$ and 97.981 GHz, respectively, was carried out using the Owens Valley Radio Observatory (OVRO) millimeter-wave array between 1991 April and 1993 May. Observations at 115.272 GHz employed three 10.4 m diameter telescopes while the 97.981 GHz maps utilized four telescopes. Each telescope was equipped with an SIS receiver, cryogenically cooled to 4 K, producing typical overall system temperatures of 520 K (SSB) at 115 GHz and 320 K (SSB) at 98 GHz.

During the CO observations, two filter banks of 32×1 MHz and 32×50 kHz provided velocity resolutions of 2.6 and 0.13 km s^{-1}. The CS spectral line observations used a digital correlator configured to provide velocity resolutions of 1.53 and 0.38 km s^{-1}. In both instances, the bandpass was centered on the cloud velocity of −18.3 km s^{-1} (Torrelles *et al.* 1983), while simultaneous continuum observations were obtained in a broadband channel of effective width ~375 MHz.

The phase and amplitude gains were calibrated by observing the quasar 0212+735 at 25 min intervals, and the absolute flux scale was established from measurements of Neptune and Uranus. Maps were generated from calibrated visibility data using the NRAO AIPS software package. Positional accuracy is ±2″. Maximum unprojected baselines of 140 m north–south and 200 m east–west gave a uniform weighted synthesized beam of 3.″8×2.″7, PA 90°, at 98 GHz and a naturally weighted beam of 7.″8×4.″8, PA 85°, at 115 GHz. For these beams, $T_B=1$ K corresponds to 0.41 and 0.08 Jy/beam. The phase center of the maps is α (1950)=$00^h33^m52.11^s$, δ (1950)=+63°12′24.″0, the position of RNO 1B (Staude & Neckel 1991).

3. CSO RESULTS AND ANALYSIS

Table 1 lists the line parameters and integrated fluxes of molecular species observed toward RNO 1B/1C with the CSO. Dashes indicate where spectra are seriously affected by self-absorption or outflow. The presence of wing emission is

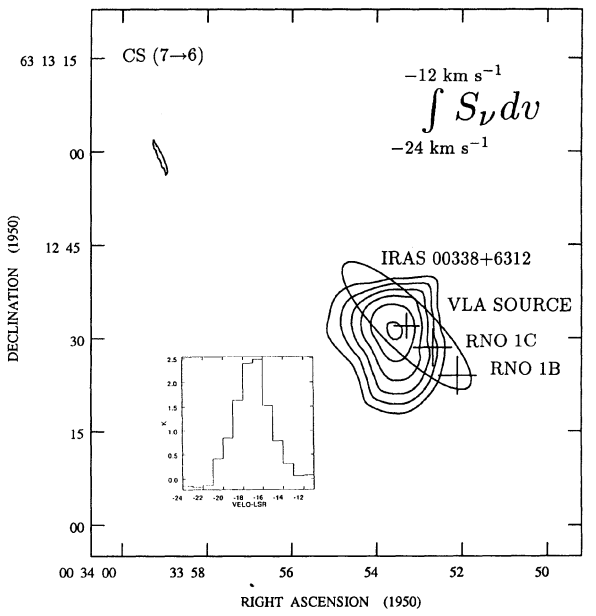

FIG. 1. A map of the CS (7→6) emission integrated between $V_{LSR}=-24$ to -12 km s^{-1}. Contours begin at 8 K and are separated by 1 K. The inset shows the CS spectrum in the region of peak emission. A cross 4″ in size marks the position of the VLA source while an ellipse indicates the range of positional uncertainty for IRAS 00338+6312. Crosses 6″ in size mark the positions of RNO 1B and RNO 1C.

indicated in column 8, where a question mark indicates too low a signal-to-noise ratio to detect outflow signatures. The velocity of peak flux is indicated in column 6; molecules with low critical densities, such as CO and its isotopes, peak at ~ -18.3 km s^{-1}, while species with higher critical densities have maxima between -17.6 and -15.7 km s^{-1}. Where collisional cross sections were available, column densities and fractional abundances were calculated using an LVG code. Otherwise, an LTE code in the optically thin regime was employed.

3.1 The Cloud Core

Contours in Fig. 1 show the CS (7→6) emission integrated over the velocity range -24 to -12 km s^{-1}. Contours begin at 20% of the peak flux of 13 K km s^{-1} and are separated by 10%. Emission is marginally resolved in the 21″ beam. The peak is displaced ~4″ southwest of the IRAS position and ~12″ northwest of RNO 1C. As the spectrum inset in Fig. 1 shows, the line peaks at a velocity of -17.0 km s^{-1}. Excitation of the CS (7→6) transition requires densities in excess of 10^6 cm^{-3}, so that the observations trace a high density core surrounding the FUors displaced from the bulk cloud velocity of -18.3 by 1.3 km s^{-1}. We therefore adopt -17.0 km s^{-1} as the systemic velocity of the core containing the FUors.

The spectra of most species, apart from the CO isotopes, also peak near -17.0 km s^{-1} implying an origin within the CS core. Calculations utilizing an LVG code and the ratio of the H_2CO line pair indicate a kinetic temperature, T_{kin}, of 30–40 K. At these temperatures, the ratio is only weakly dependent on density, making this a particularly useful temperature diagnostic (cf. Jansen *et al.* 1993; van Dishoeck *et al.* 1993a, b; Mangum & Wootten 1993). LTE calculations yield similar values, 30–50 K. Columns 10 and 11 in Table 1 list the range of fractional abundances for each molecular species, determined by dividing species column density by the molecular hydrogen column density of the cloud and of the outflow, respectively. In column 10, lower limits are derived by dividing by the molecular hydrogen column density estimated from $C^{18}O$ measurements which trace the total mass in the core and surrounding cloud, assuming a canonical abundance $C^{18}O/H_2=2\times10^{-7}$ (Chackerian & Tipping 1983). In column 11, upper limits are derived by dividing by the molecular hydrogen column density estimated from the CO (3→2) wing column density of 2×10^{17} cm^{-2}, using $^{12}CO/H_2=10^{-4}$ (Chackerian & Tipping 1983) and assuming that emission originates entirely from outflowing gas. For comparison, column 12 lists fractional abundances for the cold core TMC 1 (van Dishoeck *et al.* 1993a, b, and references therein). In calculating the core mass, we adopt a CS abundance ratio typical of dense cores and intermediate between our two derived extremes of $CS/H_2=1\times10^{-8}$ (Irvine *et al.* 1987). For $T_{kin}=35$ K, we calculate a core column density of 2.0×10^{22} cm^{-2} in the optically thin limit, leading to a core mass, $\mathcal{M}_{core}$, of 2.6 $\mathcal{M}_\odot$.

Figure 2 displays the ^{12}CO, ^{13}CO, and $C^{18}O$ (2→1) spectra at the position of RNO 1B. The CO (and HCO^+) spectrum shows a self-absorption minimum centered at -17.0 km s^{-1}, suggesting absorption is associated with a lower excitation cocoon surrounding the core seen in the CS (7→6) map. This feature is not observed in lower spatial resolution CO spectra (Yang *et al.* 1991), consistent with a localized absorbing layer.

3.2 Cloud Characteristics

Due to their low critical densities, $n_{crit}\sim10^3$ cm^{-3}, emission from the $J=2\rightarrow1$ transition of ^{13}CO and $C^{18}O$ molecules probably traces the ambient, larger-scale cloud structure. In both species, the spectra peak near -18.3 km s^{-1}. Linewidths are about 2.7 km s^{-1} away from RNO 1B/1C, increasing to 3.4 km s^{-1} in the direction of the FUors. From the ratio of $^{13}CO/C^{18}O$ peak brightness temperatures, we estimate the $C^{18}O$ optical depth, $\tau_{C^{18}O}$, is 0.4. LVG calculations, using the $C^{18}O$ line parameters 42″ away from the core center, yield a cloud column density of 5×10^{22} cm^{-2}, assuming a standard abundance ratio of $C^{18}O/H_2=2\times10^{-7}$ (Chackerian & Tipping 1983).

3.3 Outflow Characteristics

In Fig. 2, the strong wing emission in ^{12}CO is not evident in $C^{18}O$, while ^{13}CO exhibits only a weak blueshifted wing. Comparison of CO and $C^{18}O$ spectra suggests inner velocity boundaries to the outflow wings of -20 and -15 km s^{-1}, excluding velocities effected by self-absorption, and similar to estimates based on CO (3→2) measurements at 21″ resolution (Evans *et al.* 1994). To investigate the outflow further, we mapped the CO (3→2) line at 10″ spacings over the region where wings were clearly evident. Emission was de-

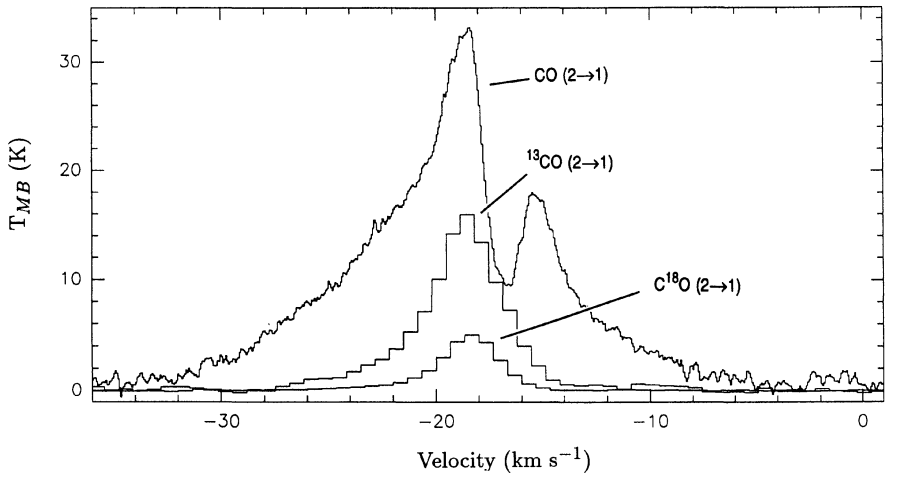

FIG. 2. Line emission in CO, ^{13}CO, and C^{18}O (2→1) as detected at the CSO. Temperatures have been corrected for main beam efficiencies.

tected only between −37 and −3 km s^{-1} to a 3σ limit of 0.9 K. Self-absorption is clearly evident between −19.5 and −15 km s^{-1}. In Fig. 3, broken contours depict the blueshifted CO (3→2) component integrated over the velocity range −37 to −20 km s^{-1}. Solid contours delineate the weaker redshifted emission integrated between −15 and −3 km s^{-1}. Taken together, the blue and redshifted CO (3→2) emission regions trace a bipolar outflow extending ~90″ tip to tip along PA ~45°. The morphology is similar to that observed in CO (1→0) maps (Snell *et al.* 1990; Yang *et al.* 1991) and in the less completely sampled CO (3→2) observations of Evans *et al.* (1994). The positions of IRAS 00338 +6312, RNO 1C, and RNO 1B are located between the redshifted and blueshifted emission peaks, implying, as expected, that one of them is the driving source of the outflow.

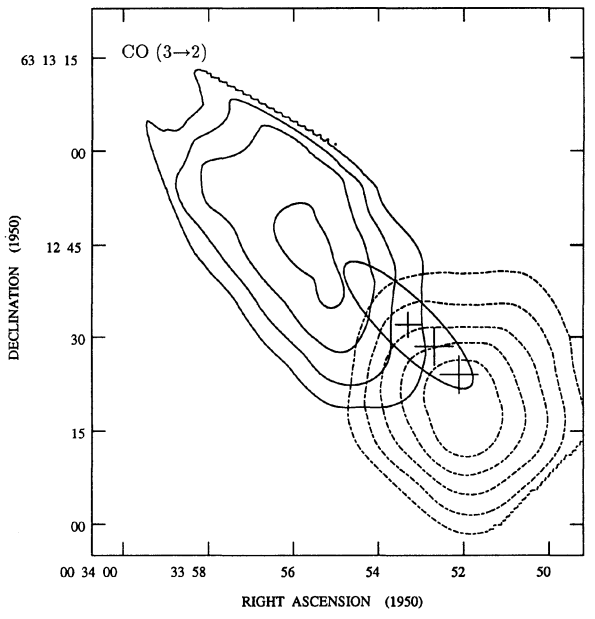

FIG. 3. A map of the CO (3→2) emission observed at the CSO. Broken contours depict the blueshifted emission, peak 149 K km s^{-1}, integrated between velocities of −37 and −20 km s^{-1}. Solid contours depict the redshifted emission, peak 114 K km s^{-1}, integrated between velocities −15 and −3 km s^{-1}. In both cases, contours begin at 50 K km s^{-1} and are spaced by 20 K km s^{-1}.

Following Scoville *et al.* (1986), we calculate the mass in each outflow lobe from the equations

$$\int N(\mathrm{CO})\,d\Omega = 4.75\times10^{12}\,\frac{(T_x+0.93)}{e^{-22.34/T_x}} \times \frac{\tau_{\mathrm{CO}}}{(1-e^{-\tau_{\mathrm{CO}}})}\int\int T_{\mathrm{MB}}\,dv\,d\Omega \qquad (1)$$

and

$$\mathcal{M} = 4.04\times10^{9}\,\frac{\mu m_{\mathrm{H_2}}(D_{\mathrm{kpc}})^2 \int N(\mathrm{CO})\,d\Omega}{X(\mathrm{CO})}\,\mathcal{M}_\odot. \qquad (2)$$

Here, $\int\int T_{\mathrm{MB}}\,dv\,d\Omega$ is the integrated line intensity summed over the solid angle $d\Omega$ for which emission is apparent, and has values of 2.1×10^{-6} and 3.6×10^{-6} K km s^{-1} sr^{-1} for the blue and red wings, respectively. T_x is the excitation temperature; τ is the optical depth; μ is the mean molecular weight; $m_{\mathrm{H_2}}$ is the mass of molecular hydrogen; D is the source distance in kiloparsecs, and X(CO) is the CO abundance relative to hydrogen. We adopt $X(\mathrm{CO})=10^{-4}$ (Chackerian & Tipping 1983) and an average excitation temperature of 15 K, the typical kinetic temperature in the outflow. A 5 K temperature difference corresponds to an approximate 20% change in mass. Optical depths of 9.2 and 3.1 for the blue and red wings are calculated from the CO/^{13}CO (3→2) brightness ratio (Evans *et al.* 1994), with resulting masses of 1.4 and 0.5$\mathcal{M}_\odot$. Using flux weighted average outflow velocities of −6.5 and +3.5 km s^{-1} relative to the systemic velocity, we estimate the momenta in the blue and red lobes to be 9.1 and 1.8$\mathcal{M}_\odot$ km s^{-1}.

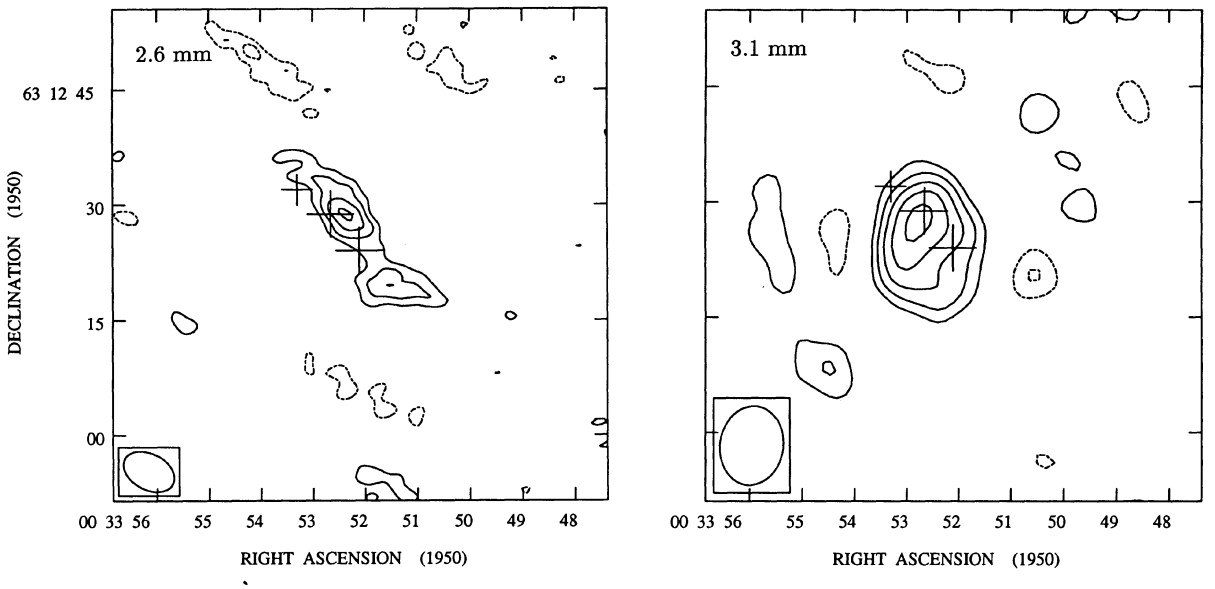

FIG. 4. Aperture synthesis maps of the 2.6 and 3.1 mm continuum emission observed toward RNO 1B/1C. Contours begin at the 2σ level of 11 and 9 mJy/beam at 2.6 and 3.1 mm, respectively, and are thereafter separated by 1σ. An ellipse in the lower left corner denotes the size of the synthesized beam in all OVRO maps. In this and all subsequent maps, the error ellipse of the *IRAS* source position is omitted to minimize confusion.

4. OWENS VALLEY RESULTS AND ANALYSIS

4.1 Continuum Emission in the Core

Figures 4(a) and 4(b) show maps of the 2.6 and 3.1 mm continuum flux in the vicinity of RNO 1B/1C. Extended flux is at low signal to noise levels at 3.1 mm and contaminated by sidelobes at 2.6 mm. Morphological differences between the two maps are strongly affected by the beam pattern since emission in the central core is only marginally resolved in each case, with a 7.″0×4.″0 (PA 37°) beam at 2.6 mm and a 10.″4×8.″2 (PA −8°) beam at 3.1 mm. Within the positional errors of ±2″, both the 2.6 mm peak of 26 mJy/beam and the 3.1 mm peak of 29 mJy/beam coincide with RNO 1C. This strongly suggests that emission from RNO 1C dominates the emission pattern. High resolution maps of millimeter continuum emission are probably the most reliable way of identifying embedded thermal sources (cf. Sargent & Welch 1994).

VLA observations at λ=3.6 and 6 cm revealed a source near the *IRAS* position with spectral index 1.5, typical of ionized gas (McCutcheon *et al.* 1991; Anglada *et al.* 1994). Extrapolation indicates that such free–free processes contribute less than 6 mJy at λ=3.1 mm. Our aperture synthesis maps therefore trace thermal dust emission. The concentration of dust towards RNO 1C suggests that this source is possibly the primary driver of the outflow.

Following Hildebrand (1983), the mass of molecular gas associated with RNO 1C can be calculated from the 2.6 and 3.1 mm flux densities of 60±30 and 45±20 mJy, respectively, using

$$\mathcal{M}_{H_2}=\frac{0.120F_{Jy}(D_{kpc})^2(\lambda_{mm})^3(e^{14.4/\lambda_{mm}T_d}-1)}{\kappa_\nu}\mathcal{M}_\odot, \quad (3)$$

where F_{Jy} is the observed continuum flux density in Janskys, λ_{mm} is the observing wavelength in millimeters, T_d is the dust temperature, and κ_ν is the mass opacity coefficient for the dust grains at frequency ν. We assume a characteristic dust temperature of 50 K, slightly larger than our value for the core kinetic temperature of 35 K. Estimates of κ_ν can vary by over an order of magnitude. Here we adopt

$$\kappa_\nu=\kappa_0\left(\frac{0.25\ \text{mm}}{\lambda_{mm}}\right)^\beta, \quad (4)$$

with $\kappa_0=0.1\ \text{cm}^2\,\text{gr}^{-1}$ (Hildebrand 1983) and $\beta\sim1$ (cf. Beckwith & Sargent 1991). Resulting masses are 1.1±0.6 and 1.4±0.6$\mathcal{M}_\odot$ at 2.6 and 3.1 mm. This value of κ_ν is conservatively high, giving lower limits to the mass surrounding RNO 1C. Upper limits to the mass, using the same coefficients, at the positions of RNO 1B and the VLA source are 0.3 and 0.4$\mathcal{M}_\odot$, at 2.6 and 3.1 mm, respectively.

4.2 CO (1→0) Maps

Figures 5(a)–5(d) show aperture synthesis CO (1→0) line maps of the RNO 1C region at ∼5″ resolution in the velocity ranges −44.2 to −31.2, −31.2 to −23.4, −23.4 to −18.2, and −15.6 to −5.2 km s^{-1}. No flux was detected outside these velocity ranges to a 3σ limit of 240 mJy/beam. At the highest blueshifted velocities, Fig. 5(a), the peak flux is centered between RNO 1C and RNO 1B; at smaller blueshifted velocities, Figs. 5(b) and 5(c), emission extends away from the stars to the southwest. At low redshifted velocities seen in Fig. 5(d), emission peaks to the northeast of RNO 1C. Taken together, these features form the blue and redshifted

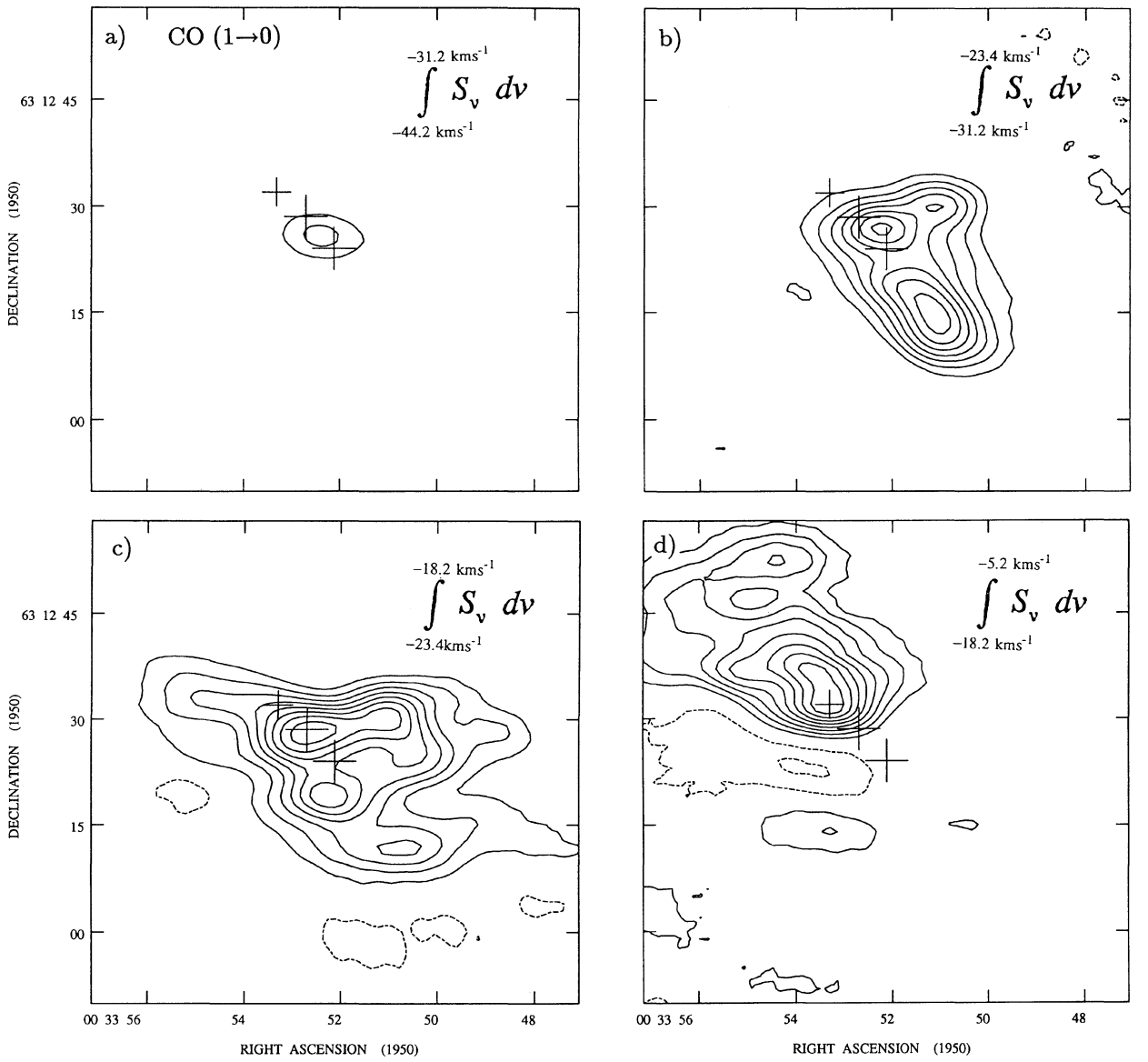

FIG. 5. Maps of the CO (1→0) emission observed by the OVRO integrated over the velocity ranges −44.2 to −31.2, −31.2 to −23.4, −23.4 to −18.2, and −18.2 to −5.2 km s^{-1}. Contours begin at and are separated by 0.5 Jy/beam km s^{-1}.

components of the bipolar outflow. In our CSO CO (3→2) maps, the blueshifted lobe also extends to the southwest and the redshifted lobe to the northeast, so that highly blueshifted CO (1→0) emission is expected southwest of the driving source, reaffirming the central role of RNO 1C. Indeed, as shown in Fig. 5(c), emission near the core velocity peaks within the positional uncertainties at RNO 1C. Strong extended emission lies along PA 115°, approximately perpendicular to the outflow. It is unclear from the present data if this is a disk-like structure or part of the outflow.

The total integrated fluxes for each of the regions depicted in Figs. 5(a)–5(d) are 15, 233, 401, and 339 Jy km s^{-1}, respectively. Following Scoville *et al.* (1986), the mass of H_2 implied in each case is given by

$$\mathcal{M} = 2.19\times10^{-9}\,\frac{(T_x+0.93)}{e^{-5.53/T_x}} \times \frac{\tau_{CO}}{(1-e^{-\tau_{CO}})}\,\frac{D_{kpc}^2}{X(CO)}\int S_\nu\,dv\ \ \mathcal{M}_\odot, \qquad (5)$$

where $\int S_\nu\,dv$ is the integrated flux density in units Jy km s^{-1} and the remaining parameters are as described for Eq. (1). As before, we adopt an excitation temperature for the outflow of 15 K and assume the emission is optically thin. We calculate minimum masses for the regions depicted in Figs. 5(a)–5(d) of 5×10^{-3}, 0.08, 0.15, and 0.12$\mathcal{M}_\odot$ and associated momenta of 0.12, 0.85, 0.55, and 0.67$\mathcal{M}_\odot$ km s^{-1}, respectively.

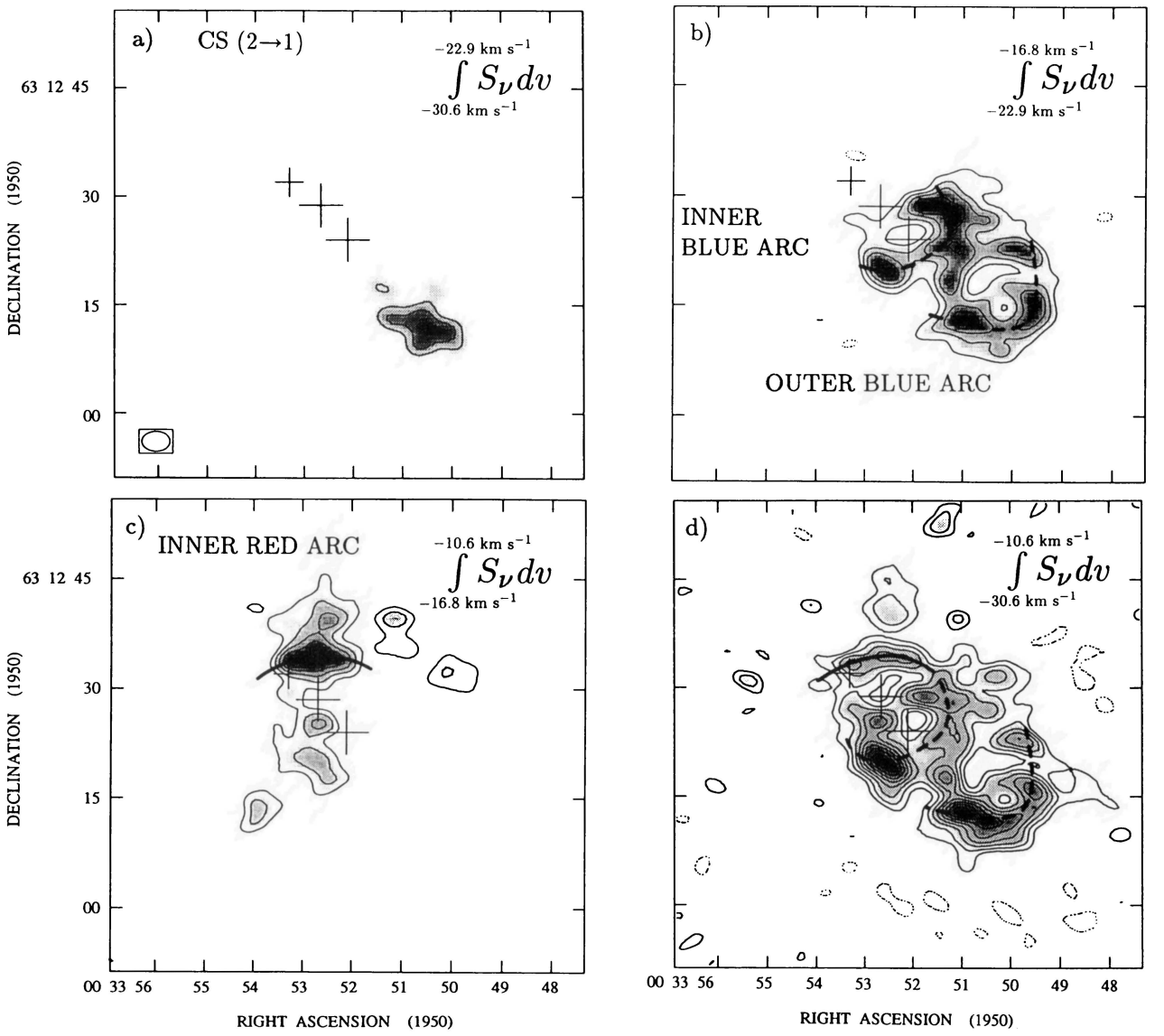

FIG. 6. Aperture synthesis maps of the CS (2→1) emission integrated over velocities −30.6 to −22.9, −22.9 to −16.8, −16.8 to −10.6, and −30.6 to −10.6 km s^{-1}, respectively. Contours in each map begin at 20% of the peak total integrated flux, 3.42 Jy/beam km s^{-1}, and are separated by 10%. The greyscale image depicts the same emission for clarification. Heavy broken lines trace the blueshifted arcs described in the text while a solid line follows the redshifted arc.

4.3 CS (2→1) Emission

Emission from the CS (2→1) rotational transition was detected only between velocities of −30.6 and −10.6 km s^{-1} to a 3σ limit of 26 mJy/beam. No high velocity gas corresponding to the CO (1→0) emission seen in Fig. 5(a) was observed. The contour and greyscale aperture synthesis maps of Figs. 6(a)–6(c) show the CS integrated intensity at ~3″ resolution over the velocity ranges −30.6 to −22.9, −22.9 to −16.8, and −16.8 to −10.6 km s^{-1}. Figure 6(d) shows the total integrated CS (2→1) emission. The CS (2→1) emission peak is not coincident with the CS (7→6) maximum (Fig. 1), probably due to the lower resolution and greater positional uncertainties of the CSO data.

At the highest observed blueshifted velocities, Fig. 6(a), emission peaks ~18″ southwest of RNO 1C with a low intensity region extending back toward the star. The morphology is roughly analogous to that in the CO (1→0) map of Fig. 5(b). We infer the CS structure represents a denser component of the blueshifted outflow. In Fig. 6(b), a possible double arcuate structure lies to the southwest of the FUors; the more prominent arc is located about 25″ from RNO 1C while a possible inner arc lies within 10″. Redshifted emission shown in Fig. 6(c) peaks ~5″ north of RNO 1C and may be the redshifted counterpart of the inner arc seen in Fig. 6(b). Overall, the redshifted emission is less prominent than the blueshifted component. Indeed, our CSO observations demonstrate that the red outflow has a lower peak intensity and is slightly more extended so that it may be resolved out. Within 1 km s^{-1} of the systemic velocity, −17 km s^{-1}, emission also appears resolved out or possibly self-absorbed.

Maps presented in Fig. 7 illustrate the behavior of blueshifted CS emission between −22.32 and −18.11 km s^{-1} at

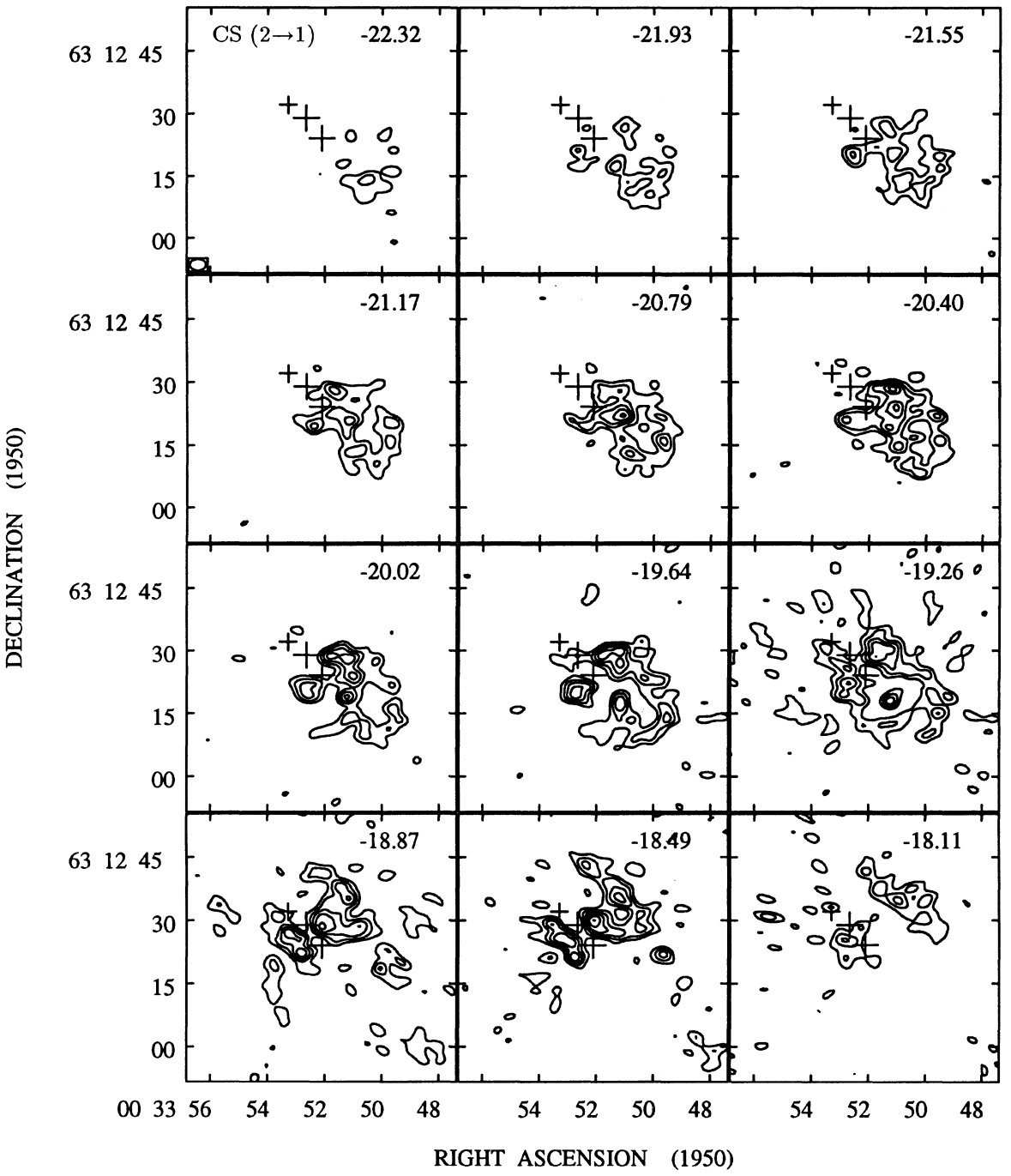

FIG. 7. High velocity resolution maps of the blueshifted CS (2→1) emission observed toward RNO 1B/1C between the velocity range −22.32 to −18.11 km s^{-1}. The velocity of each channel is indicated in the upper right corner. Contours begin at the 3σ level, 270 mJy/beam, and are thereafter separated by 2σ.

a velocity resolution of 0.38 km s^{-1}. There is a condensation 25″ southwest of RNO 1C at the highest velocities. Approaching the systemic velocity, −17 km s^{-1}, this bifurcates forming a loop. Emission is also present ~10″ to the south and west of RNO 1C and forms a possible inner arc between velocities of −21.55 and −20.02 km s^{-1}. At distances of ~10″–25″ (8.5–21.2×10^3 AU) from RNO 1C the observed velocity displacements are not consistent with rotation or infall. We suggest emission arises from outflowing gas. Between −19.64 and −18.49 km s^{-1}, the morphology is dominated by a dumbbell structure oriented perpendicularly to the outflow. For these velocities which are closer to the systemic value, it is difficult to ascertain whether emission arises from rotation, infall, or outflow.

The mass of swept up gas can again be calculated (cf. Scoville *et al.* 1986; Ohashi *et al.* 1991) using

$$\mathcal{M} = 1.3\times10^{-11}\,\frac{(T_x+0.4)}{e^{-7.1/T_x}} \times \frac{\tau_{CS}}{(1-e^{-\tau_{CS}})}\,\frac{D_{kpc}^2}{X(CS)}\int S_\nu\,dv\;\;\mathcal{M}_\odot, \qquad (6)$$

where we use the same parameters as in for Eq. (5) but with a CS abundance ratio, X(CS), of 1×10^{-8} (Irvine *et al.* 1987). Assuming optically thin emission, we calculate masses of 0.24, 1.20, and 0.94 $\mathcal{M}_\odot$ for the structures observed in each of the velocity ranges of Figs. 6(a)–6(c). Estimated masses and momenta for the outer and inner "arcs" are 0.58 and 0.52 $\mathcal{M}_\odot$, and 2.20 and 2.08 $\mathcal{M}_\odot$ km s^{-1}.

5. DISCUSSION

5.1 Chemistry

Our CSO maps demonstrate that the FU Orionis binary system, RNO 1B/1C, is surrounded by a dense core, 1.8×10^4 AU in size, of mass $\sim3\,\mathcal{M}_\odot$. Although the core is only weakly offset from the bulk cloud velocity, outflowing gas is kinematically quite distinct from the ambient cloud material. Mass estimates of the quiescent and outflowing components are provided by the $C^{18}O$ and ^{12}CO $J=2\rightarrow1$ lines, from which we derive the fractional abundance limits presented in Table 1. For comparison, this table also presents the abundances found in the TMC 1 dark cloud.

The abundances of most molecules, especially those not obviously associated with the outflow, are comparable to those in molecular cloud cores devoid of star formation. Certain species, notably CS, H_2CO, and SO are weakly enhanced in the outflowing gas; by contrast, CH_3OH and SiO show enhancements larger than an order of magnitude. While the small enrichments may result from density and temperature enhancements caused by the outflow, the enhancements of SiO and CH_3OH are likely the result of chemical interactions.

Moderate enhancements in SiO and CH_3OH are not unusual in regions of outflow activity (cf. Bachiller & Gomez-Gonzalez 1992; van Dishoeck *et al.* 1993a, b), where low velocity shocks can drive new reaction routes even for low luminosity sources. The refractory SiO molecule is most likely produced by sputtering or evaporation of dust grains in regions of directly shocked and entrained material. The high observed abundances of CH_3OH towards RNO 1B/1C cannot be produced either by low temperature ion–molecule or gas phase shock chemistry (Sandell *et al.* 1994). However, grain mantle evaporation can provide the needed methanol (Blake *et al.* 1991); the increased velocity dispersion surrounding bipolar outflows may result in shorter grain–grain collision times at relatively low collision velocities, thereby increasing grain mantle evaporation rates without shattering the grains themselves (Blake *et al.* 1995). These two distinct processes of grain sputtering, as opposed to softer grain–grain collisions, should have different spatial distributions. However, higher spatial resolution observations are required to investigate the RNO 1B/1C morphology further.

5.2 The Driving Source of the Outflow

Aperture synthesis maps of the continuum emission at 2.6 and 3.1 mm, shown in Figs. 4(a) and 4(b), suggest a lower limit of 1.1 $\mathcal{M}_\odot$ for the mass around RNO 1C. Reprocessed radiation from the dust may account for the sharp rise in the RNO 1B/1C spectral energy distribution beyond 12 μm (Kenyon *et al.* 1993). For a source ~5000–7000 AU in size, a spherical dust distribution produces a visual extinction $A_v \geqslant 50$ mag (Spitzer 1978), much larger than the observed value of $A_v \sim 12$ mag (Staude & Neckel 1991). It seems likely that the dust is asymmetrically distributed, but the large size precludes a truly centrifugally supported circumstellar accretion disk. Since continuum emission appears marginally resolved at different beam sizes, we suggest that the material surrounding RNO 1C follows a power law density distribution (Ladd *et al.* 1991; Terebey *et al.* 1993).

The location of RNO 1C at the peak of millimeter continuum emission, its central position between the peaks of the blue and redshifted outflow lobes [Figs. 5(a)–5(d)], and its association with the CS (2→1) dumbbell structure (Fig. 7), together indicate that the FUor is the driving source for the outflow in L1287. Infrared polarization measurements and centimeter continuum emission suggest a third more embedded source near the *IRAS* position is possibly the driving source (McCutcheon *et al.* 1991; Weintraub & Kastner 1993; Anglada *et al.* 1994). However, the millimeter continuum peak is located ~8″ from the *IRAS* position, virtually excluding it as the outflow source, since millimeter continuum measurements are probably the most accurate determinant of the position of an embedded object. We suggest that the infrared observations are sensitive to the dust geometry surrounding RNO 1C and are therefore affected by the outflow cavity structure. Moreover, the radio emission spectral index of 1.5 is characteristic of free–free emission regions frequently observed at moderate distances from energetic, outflow sources (McMullin *et al.* 1994). The error in the *IRAS* position easily includes both RNO 1B and RNO 1C. It is difficult to reconcile the spatial coincidence of the *IRAS* source, the centimeter emission peak, and pattern of polarization with our new observations.

5.3 Outflow Structure

High spatial resolution (3.″8×2.″7, PA 90°) maps of the CS (2→1) emission reveal the high density structure of the L1287 outflow in Figs. 6(a)–6(d) and 7. We do not detect the axisymmetric offset in the outflow noted by Yang *et al.* (1993) and interpreted as evidence of helical structure. Overall, the emission pattern resembles a limb-brightened outflow cavity lying nearly in the plane of the sky. The morphology is consistent with CS emission tracing the cavity walls that have been compressed by the outflow wind and with the higher velocity CO emission tracing entrained low-density gas.

In Fig. 8(a), contours of the blueshifted CO (1→0) emission integrated between velocities −44.2 and −20.8 km s^{-1} are shown, while in Fig. 8(b), contours trace the redshifted CO emission integrated between −15.6 and −5.2 km s^{-1}. In both figures, a greyscale image shows the total integrated CS

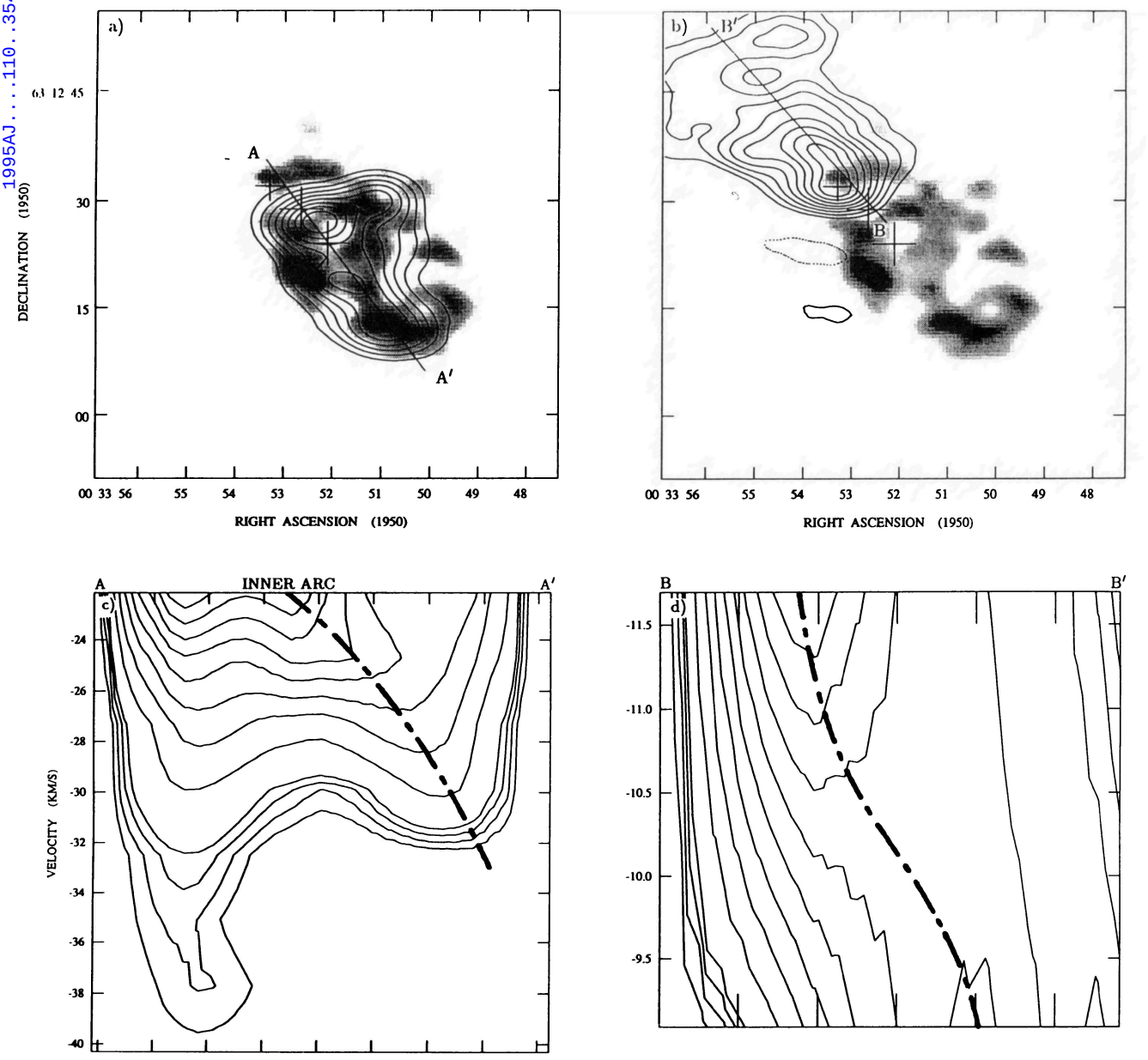

FIG. 8. Aperture synthesis maps of CO (1→0) and CS (2→1) emission towards RNO 1B/1C. Contours in (a) depict the blueshifted CO emission integrated over velocities −44.2 to −20.8 km s^{-1} while contours in (b) depict the redshifted CO emission integrated between −15.6 and −5.2 km s^{-1}. Contours start at 20% and are separated by 10% of the peak flux in each velocity interval. In both cases, the greyscale shows the total integrated CS emission. (c) and (d) are the position–velocity diagrams of emission along AA′ and BB″, respectively. Contours are at 4%, 6%, 8%, 10%, 20%, 30%, 40%, 50%, 60%, 70%, 80%, and 90% of the peak flux in each diagram. Heavy dashed lines trace the approximately linear velocity trends discussed in the text.

(2→1) emission which we believe traces the outflow cavity. The maximum blueshifted CO intensity occurs southwest of RNO 1C and extends to the southwest. Secondary peaks occur at the positions of the inner and outer arcs described in Sec. *4.3*. By contrast, redshifted CO peaks at the position of the northern inner arc and extends to the northeast. Figures 8(c) and 8(d) are position–velocity (PV) cuts through the blue and red lobes along lines AA′ and BB′, respectively. It is clear from Fig. 8(c), that gas over a wide velocity range contributes to the emission around RNO 1C labelled as Region 1. Across the southern inner arc, emission appears at velocities between ∼−22 and −32 km s^{-1}. Between the arcs, peak velocity linearly increases with distance from the source as marked by a dashed line. A similar although much weaker trend is apparent for the redshifted emission in Fig. 8(d).

Although outflow models predict the existence of cavities (Masson & Chernin 1993; Raga & Cabrit 1993; Chernin *et al.* 1994), few have been confirmed (Uchida *et al.* 1987; Moriarty-Schieven *et al.* 1987; Avery *et al.* 1990; Meyers-Rice & Lada 1991). There is some suggestion that cavities around FUors may be more common (Moriarty-Schieven *et al.* 1987; McMuldroch *et al.* 1993). In terms of time scales and velocities characteristic of outflows, a FUor event is explosive and instantaneous. The inner and outer arcs traced in CS (2→1) may be interpreted as dense gas swept up by two separate FUor outbursts. Material is driven at all velocities by an outburst, which becomes velocity sorted with increas-

ing distance from the source, leading to the PV structures seen in Figs. 8(a) and 8(b). Gas swept up by the more recent outburst lies close to the source at all velocities, while velocity sorting of the gas swept up earlier has produced the observed linear position–velocity relationship. Alternatively, the observed velocity pattern can be interpreted in terms of time-dependent collimated jet outflow models (Raga & Biro 1993; Raga & Cabrit 1993), in which internal working surfaces propagate along a collimated jet entraining gas in the wake of a bowshock. These models produce cavity morphologies comparable to those presented here and also yield radial velocities that increase away from the source. However, these models are for outflows with a time-dependent wind velocity rather than mass loss rate as is the case for FUors.

The momenta of the cavity's inner and outer arcs, estimated from measurements of CS (2→1) emission, are 2.0 and 2.1 $\mathcal{M}_\odot$ km s^{-1}, respectively, while the momenta of the CO (1→0) outflow lobes are 1.6 and 1.0 $\mathcal{M}_\odot$ km s^{-1}. A classical FUor outburst lasting 100 yr, with a wind velocity of 500 km s^{-1} and a mass loss rate of 10^{-4} $\mathcal{M}_\odot$ yr^{-1}, imparts only ~0.5 $\mathcal{M}_\odot$ km s^{-1} of momentum. This suggests that if the arcs were formed by FUor activity then the outbursts were exceptionally energetic entraining ~4 $\mathcal{M}_\odot$ km s^{-1}. The present luminosity of L_{bol}~1000 $L_\odot$ for RNO 1B/1C suggests the current outburst is also exceptionally energetic, assuming wind energy scales with accretion luminosity (Cabrit & Bertout 1992).

Single dish CO (3→2) observations yield an outflow lifetime of ~10^4 yr. The velocity dispersions seen in Figs. 8(c) and 8(d) suggest a repetition time scale of 4×10^3 yr, while dynamical age estimates of the arcs, made from CS observations assuming an inclination angle i=30°, yield lower bounds of 4×10^3 and 1×10^4 yr. A maximum of three outbursts could have occurred in the lifetime of the outflow yielding ~12 $\mathcal{M}_\odot$ km s^{-1} of momentum, approximately the total outflow momentum of 11 $\mathcal{M}_\odot$ km s^{-1} (see Sec. *3.3*). If the arcs are indeed caused by FUor activity, then FUor outbursts possibly dominate both outflow morphology and outflow energetics in this source.

6. CONCLUSIONS

We have carried out sensitive high resolution millimeter and submillimeter observations of the FU Orionis binary system RNO 1B/1C. CS (7→6) measurements trace a dense core, 1.8×10^4 AU in size, mass ~3 $\mathcal{M}_\odot$, at V_{LSR}=−17.0 km s^{-1}. Fractional chemical abundances in this core, calculated from LVG and LTE codes, are largely similar to those in the cold core TMC 1. Enhancements in the SiO and CH_3OH abundances are consistent with a low velocity shock liberating grain mantle material to the gas phase. Indeed, observations of the CO (3→2) emission delineate a bipolar outflow, oriented at PA 45°, with blueshifted emission lying to the southwest of RNO 1B/1C.

Aperture synthesis observations of 2.6 and 3.1 mm continuum emission from the RNO 1B/1C core at 7.″0×4.″6 (PA 62°) and 10.″4×8.″2 (PA −8°) resolution lead us to conclude that RNO 1C is surrounded by a flattened dusty envelope, ~5000 AU in size, with a minimum mass of 1.1 $\mathcal{M}_\odot$. The morphology of the CO (1→0) aperture synthesis images also suggests RNO 1C is possibly the driving source. A dumbbell structure oriented at 90° to the outflow axis and 3″ southwest of RNO 1C is visible in CS (2→1) images and further strengthens this interpretation.

The CS (2→1) interferometer maps are consistent with the presence of an outflow cavity lying nearly in the plane of the sky. Two concentric arcs, 8×10^3 and 8×10^3 AU from RNO 1C, are apparent in blueshifted emission, although only the inner arc has a redshifted counterpart. The gas velocity structure is consistent with formation by two energetic FU Orionis outbursts, 4×10^3 and 1×10^4 yr ago. The time between outbursts, ~5×10^3 yr, is comparable to previous estimates based on source frequency statistics of 2×10^3 yr. Each outburst may have imparted ≥4 $\mathcal{M}_\odot$ km s^{-1} to the outflow implying a mass loss rate of $\dot{\mathcal{M}}$~10^{-4} $\mathcal{M}_\odot$ yr^{-1} for a 500 km s^{-1} wind lasting 100 yr. It appears that while young pre-main sequence stars are in the FU Orionis stage, outbursts may possibly dominate both outflow morphology and energetics.

We are indebted to the staff of the Owens Valley millimeter-wave array and the Caltech Submillimeter Observatory for their unfailing support and extend special thanks to Taco for his assistance with the CSO mapping software. We are extremely grateful to Ewine van Dishoeck and Todd Groesbeck for providing use of their LVG and LTE codes. We extend our thanks to the referee for many helpful suggestions. Astronomy with the Owens Valley Array is funded by NSF Grant AST 93−14079 and the CSO by NSF Grant AST 93−13929. S.M. is supported by NASA Grants NAGW-2297 and NAGW-3140, part of the Origins of Solar Systems Research Program.

REFERENCES

Anglada, G., Rodriguez, L. F., & Girart, J. M. 1994, ApJ, 420, L91
Avery, L. W., Hayashi, S. S., & White, G. L. 1990, ApJ, 357, 524
Bachiller, R., & Gomez-Gonzalez, J. 1992, A&AR, 3, 257
Beckwith, S. V. W., & Sargent, A. I. 1991, ApJ, 381, 250
Blake, D. F., Allamandola, L., Sandford, S., Hudgins, D., & Freund, F. 1991, Science, 254, 548
Blake, G. A., Sandell, G., van Dishoeck, E. F., Groesbeck, T. D., Mundy, L. G., & Aspin, C. 1995, ApJ, 441, 689
Cabrit, S., & Bertout, C. 1992, A&A, 261, 274
Chackerian, C., & Tipping, R. H. 1983, J. Molec. Spectrosc., 99, 431
Charnley, S. B. 1994, ApJ (submitted)
Chernin, L., Masson, C., & Pino, E. M. G. D. 1994, ApJ, 426, 204
Ellison, B. E., & Miller, R. L. 1987, Int. J. Infrared and Millimeter Waves, 8, 608
Ellison, B. E., Schaffer, P. L., Schaal, W., Vail, D., & Miller, R. E. 1989, Int. J. Infrared and Millimeter Waves, 10, 937
Estalella, R., Mauersberger, R., Torrelles, J. M., Anglada, G., Gomez, J. G., Lopez, R., & Muders, D. 1993, ApJ, 419, 698
Evans III, N. J., Balkum, S., Levreault, R. M., Hartmann, L., & Kenyon, S. 1994, ApJ (in press)

Fiebig, D., Duschl, W. J., & Tscharnuter, W. M. 1992, IAU Circ. 5438, 1
Goodrich, R. W. 1987, PASP, 99, 116
Hartmann, L. 1992, in NATO ASI on The Formation and Evolution of Stars, edited by N. Kylafis and C. Lada
Hartmann, L., & Kenyon, S. J. 1985, ApJ, 299, 462
Hartmann, L., & Kenyon, S. J. 1987, ApJ, 312, 243
Hartmann, L., Kenyon, S. J., & Hartigan, P. 1993, in Protostars and Planets III, edited by E. H. Levy and J. I. Lunine (University of Arizona, Tucson)
Herbig, G. H. 1977, ApJ, 217, 693
Herbig, G. H. 1989, in ESO Workshop on Low-Mass Star Formation and Pre-Main Sequence Objects, edited by B. Reipurth (ESO, Garching), p. 233
Hildebrand, R. H. 1983, QJRAS, 24, 267
Irvine, W. M., Goldsmith, P. F., & Hjalmarson, Å 1987, in Interstellar Processes, edited by D. Hollenbach and H. A. Thronson (Reidel, Dordrecht)
Jansen, D. J., van Dishoeck, E. F., & Black, J. H. 1994, A&A, 282, 605
Kenyon, S. J., Hartmann, L., Gomez, M., Carr, J. S., & Tokunaga, A. 1993, AJ, 105, 1505
Ladd, E. F., Adams, F. C., Casey, S., Davidson, J. A., Fuller, G. A., Harper, D. A., Myers, P. C., & Padman, R. 1991, ApJ, 382, 555
Mangum, J., & Wootten, A. 1993, ApJS, 89, 123
Masson, C. R., & Chernin, L. M. 1993, ApJ, 414, 230
McCutcheon, W. H., Dewdney, P. E., Purton, C. R., & Sato, T. 1991, AJ, 101, 1435
McMuldroch, S., Sargent, A. I., & Blake, G. A. 1993, AJ, 106, 2477
McMullin, J. P, Mundy, L. G., Wilking, B. A., Hezel, T., & Blake, G. A. 1994, in preparation
Meyers-Rice, B. A., & Lada, C. J. 1991, ApJ, 368, 445
Moriarty-Schieven, G. H., Snell, R. L., Strom, S. E., Schloerb, F. P., Strom, K. M., & Grasdalen, G. L. 1987, ApJ, 319, 742
Ohashi, N., Kawabe, R., Hayashi, M., & Ishiguro, M. 1991, AJ, 102, 2054
Raga, A. C., & Biro, S. 1993, MNRAS, 264, 758
Raga, A., & Cabrit, S. 1993, A&A, 278, 267
Reipurth, B. 1992, A&A, 257, 693
Sandell, G., Knee, L. B. G., Aspin, C., Robson, I. E., & Russell, A. P. G. 1994, A&A (submitted)
Sargent, A. I., & Welch, W. J. 1993, ARA&A, 31, 297
Scoville, N. Z., Sargent, A. I., Sanders, D. B., Claussen, M. J., Masson, C. R., Lo, K. Y., & Phillips, T. G. 1986, ApJ, 303, 416
Snell, R. L., Dickman, R. L., & Huang, Y.-L. 1990, ApJ, 352, 139
Spitzer, L. 1978, Physical Processes in the Interstellar Medium (Wiley, New York)
Staude, H. J., & Neckel, Th. 1991, A&A, 244, L13
Terebey, S., Chandler, C. J., & Andre, P. 1993, ApJ, 414, 759
Torrelles, J. M., Rodríguez, L. F., Cantó, J., Marcaide, J., & Gyulbudaghian, A. L. 1983, RMxA, 8, 147
Uchida, Y., Kaifu, N., Shibata, K., Hayashi, S. S., Hasegawa, T., & Hamatake, H. 1987, PASJ, 39, 907
van Dishoeck, E. F., Blake, G. A., Draine, B. T., & Lunine, J. I. 1993a, in Protostars and Planets III, edited by E. H. Levy and J. I. Lunine (University of Arizona, Tucson)
van Dishoeck, E. F., Jansen, D. J., & Phillips, T. G. 1993b, A&A, 279, 541
Weintraub, D. A., & Kastner, J. 1993, ApJ, 411, 767
Welty, A., Strom, S., Edwards, S., Kenyon, S. J., & Hartmann, L. 1992, ApJ, 397, 260
Yang, J., Umemoto, T., Iwata, T., & Fukui, Y. 1991, ApJ, 373, 137
Yang, J. Ohashi, N., & Fukui, Y. 1993, in Second Northeast-Asian Regional Meeting on Recent Development in Millimeter-Wave and Infrared Astronomy, edited by S. H. Cho and H. S. Chung (Korea Astronomy Observatory, Daejon)